doi: 10.82124/CEAS-GNC-2026-099 CEAS-GNC-2026-099

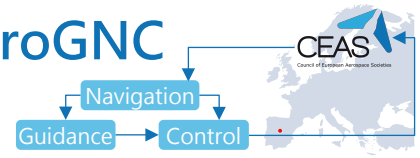

Madrid, Spain May 5th-7th 2026
uc3m Universidad Carlos III de Madrid
AIAA

Longitudinal Load Alleviation Control and Modeling of a High-Aspect Ratio Wing Flexible Aircraft

Ralf A. Senger Franco Researcher, Technical University of Berlin, Berlin, Germany. r.sengerfranco@tu-berlin.de

Willi Mickein Researcher, Technical University of Berlin, Berlin, Germany. w.mickein@tu-berlin.de

Álvaro A. G. Quesada Researcher, Technical University of Berlin, Berlin, Germany. garcia.quesada@tu-berlin.de

Pedro J. González Post Doc, Technical University of Berlin, Berlin, Germany. p.gonzalez.ramirez@tu-berlin.de

Guilherme C. Barbosa Post Doc, Technical University of Berlin, Berlin, Germany. g.chaves.barbosa@tu-berlin.de

Flávio J. Silvestre Professor, Technical University of Berlin, Berlin, Germany. flavio.silvestre@tu-berlin.de

Kilian Streitenberger Researcher, German Aerospace Center, Göttingen, Germany. kilian.streitenberger@dlr.de

Wolf-Reiner Krüger Professor, German Aerospace Center, Göttingen, Germany. wolf.krueger@dlr.de

ABSTRACT

The reduction of carbon emissions drives future aviation towards more environmentally friendly aircraft design, leading to the demand for new technologies. One crucial technology is the investigation to increase aerodynamic efficiency by reducing induced aerodynamic drag, resulting in lower fuel consumption. This is achieved by increasing the aspect ratio of the wings and using lighter materials, leading to a more flexible structure and a challenging problem due to the coupling between aeroelasticity and flight dynamics. For this reason, active load control is essential to enable high-aspect ratio wings. In this paper, we analyze the load alleviation problem for a very flexible aircraft with high aspect-ratio wings. For longitudinal load control, an autopilot including a base controller for flight dynamics and an optimal load alleviation control function are developed by modifying the performance index to directly penalize the wing root bending moment. The proposed methodology is adaptable to different feedback control laws and suitable for parametric analysis by varying the wing root bending moment weighting. Furthermore, a first order linear time-invariant actuator model with a cut-off frequency of 6 Hz and a time delay of 60 ms by means of a second order Padé approximation in the GLA feedback loop are considered. The control laws are tested in a non linear simulation environment, achieving reductions in wing root bending moment of up to 11.88 %, which is proportional to potential structural mass savings. This framework provides significant improvements for the early design phases of the next generation of more environmentally friendly aircraft.

Keywords: Active Load Control, Gust Load Alleviation, Flight Dynamics, Flexible Aircraft, High-Aspect Ratio

Nomenclature

A, B, C, D	=	state matrix, input matrix, output matrix and feedthrough matrix of a state-space system
a	=	acceleration
CAS	=	control augmentation system
$F_A^{(C)},\ F_A^{(NC)}$	=	vectors of circulatory and non circulatory aerodynamic forces
F^{ext}	=	vector of external forces
GLA	=	gust load alleviation
H	=	altitude
HARW	=	high-aspect ratio wing
IMU	=	inertial measurement unit
J	=	inertia tensor
LQR	=	linear quadratic regulator
M^{ext}	=	vector of external moment
$M_A^{(C)},\ M_A^{(NC)}$	=	vectors of circulatory and non circulatory aerodynamic moments
MLA	=	maneuver load alleviation
MTOW	=	maximum take-off weight configuration
m	=	mass
$p,\ q,\ r$	=	inertial angular rates of the body reference frame, in the body coordinate system
Q_η	=	vector of generalized loads
QS	=	quasi-steady
US	=	unsteady
WRBM	=	wing root bending moment
WRTF	=	wing root transversal force
w	=	wind velocity
V	=	velocity
SAS	=	stability augmentation system
$T_{B^{(G)}I}$	=	transformation matrix from inertial reference frame to global body reference frame
u	=	vector of control/input variables
X	=	vector of states
Y	=	vector of outputs
α	=	angle of attack of the body reference frame
β	=	angle of sideslip of the body reference frame
δ	=	control surface inputs/deflections
$\eta,\ \dot{\eta}$	=	vector of modal amplitudes
γ_k^{EA}	=	equivalent kth modal torsion at elastic axis positive pitch down
λ	=	aerodynamic lag state
μ	=	diagonal matrix of modal masses
ω_n	=	diagonal matrix of undamped natural frequencies
$\Theta,\ \Phi,\ \Psi$	=	pitch, roll and heading angles
φ_k^{EA}	=	equivalent kth modal displacement at elastic axis
ξ	=	structural/modal damping
Subscripts		
BCS	=	body coordinate system
CG	=	center of gravity
CP	=	cockpit

CS	=	control surface
HE	=	horizontal empennage
LON	=	longitudinal
LPAX	=	last PAX position
W	=	wing
VE	=	vertical empennage

1 Introduction

The next generation of commercial aircraft will include new technologies to reduce the environmental impact by reducing fuel consumption and hence carbon emissions. One of these crucial technologies aims to increase aerodynamic efficiency by reducing induced aerodynamic drag, which leads to less fuel consumption [1]. This improvement of aerodynamic efficiency is achieved by increasing the aspect ratio of the wings and by using lighter materials, resulting in an overall more flexible structure. However, such designs inherently increase structural flexibility, increasing the coupling between rigid body dynamics and aeroelastic modes. This coupling can potentially destabilize flight dynamics and flexible modes. In particular, high-aspect ratio configurations can trigger Short Period coupling with the first bending mode under certain flight conditions, a phenomenon with critical implications for safety and certification. Past incidents, such as the NASA Helios mishap [2], highlight the risks of overlooking this interaction, while studies on very flexible aircraft like the X-HALE [3] and the non linear investigations of Patil and Hodges [4] demonstrate how elastic modes can couple with rigid body dynamics. This behavior is critical to be considered within the design of load alleviation control functions for high-aspect ratio wing flexible aircraft. This concept is investigated in the research project Ultra Performance Wing (UP Wing), targeting fuel burn reductions of up to 30 % compared to a state of the-art aircraft [5]. To achieve this target, novel active load control technologies are essential to mitigate the critical load increase acting on the structure of the flexible high-aspect ratio wing.

The field of active load alleviation has evolved over decades. Early approaches in the 1970s and 1980s focused on active load alleviation concepts, culminating in the first onboard GLA system in the Airbus A320, capable of up to 15% wing root load reduction through static control surface deflections [6]. Research in the 1980s also established the theoretical framework for aeroservoelastic modeling techniques, most notably Waszak and Schmidt (1988), who formalized the coupling of rigid and flexible dynamics into the formulation of unified state-space models [7]. In the 1990s and 2000s, studies such as conducted by McLean et al. [8] expanded optimal control theory methods to large transport aircraft and Patil & Hodges highlighted the non linear behavior of rigid flexible interactions. With advances in modeling and computation, the 2010s brought more sophisticated control concepts. Cesnik and co-authors developed and flight tested the very flexible demonstrator X-HALE, showing the necessity of aeroservoelastic control for stability in high-aspect ratio wings [3]. In the last decade, new control synthesis methods for GLA emerged: Xu (2011) [9] showed first effects of GLA and MLA systems, while Silvestre et al. (2017) [10] investigated control synthesis considering the observation of the flexible states of the aircraft for active load control. Fezans et al. (2019) [11] and Wallace et al. (2024) [12] investigated feedforward load control laws based on LIDAR gust measurement. Recent works further advanced optimal and model predictive approaches: Fournier et al. (2022) [13] on robust GLA, and Wüstenhagen (2023) [14] on model predictive control for flexible aircraft with different mass distributions. Collectively, these efforts underline the importance of embedding load alleviation control early in the design of future transport aircraft, but few explicitly consider its simultaneous effect on aeroelastic and flight dynamic stability, and even fewer provide a framework readily for integration into higher complexity simulation environments.

The objective of this paper is to address this gap by developing a straightforward active longitudinal

load control methodology for a high-aspect ratio flexible aircraft and analyzing its effect on aeroelastic and flight dynamic stability. The reference study case is the DLR-F25, developed within the federal research program VirEnfREI, with an aspect ratio of 15.6 [15]. For this purpose the control laws are divided into 2 separated tasks. The autopilot considering a base controller is developed as in [16] to control the flight dynamics and provide tracking capabilities for altitude and velocity. The SAS and CAS (base controller) are derived with Eigenstructure Assignment as in [16] and [17]. The task of active load control for GLA is addressed by the wing control surfaces, in addition to the autopilot, by means of LQR output feedback as in [18]. Within this synthesis procedure the performance index is modified to target the WRBM and WRTF. This methodology is additionally developed as a tool to assess parametrically the variation of WRBM penalization in dependency of required control effort and load reduction. This framework provides the baseline of the active load control law synthesis procedure to derive the control laws prepared for embedment into the higher complexity CFD simulation environment UltraFLoads, to simulate gust encounters [19].

Optimal control law synthesis methods for GLA with output feedback have been proposed and studied in [8] applied to the Lockheed C-5a aircaft of an aspect ratio of 8, differing considerably in structural properties and aspect ratio to the current research aircraft DLR-F25. This work essentially proved proper functionality of the proposed optimal control laws. However, the current investigation is extended by the flexible high-aspect ratio study case, as well as by the augmented and modified performance index of the optimal control law by a weighting variation of the penalization parameter. In addition, the mentioned assessment capability enhances the control law synthesis procedure by providing several different controllers for a given feedback structure. Furthermore, a control law robustness evaluation is included within the proposed methodology. Due to its simplicity, different feedback structures, for using different sensor signals towards different control surfaces can be evaluated in a straightforward manner. The proposed methodology is able to provide active load control laws, achieving significant load alleviation in non linear simulations. This framework for deriving the control laws with available measurements from IMU's is therefore suitable for embedment into real aircraft applications.

The structure of this paper is as follows. Section 2 and 3 introduce the formulations and the employed control techniques for flexible aircraft. Section 4 presents the reference aircraft DLR-F25. Section 5 presents the applied control methodology and its effectiveness, followed by the conclusions in Section 6.

2 Flight Dynamics Model of a HARW Aircraft

2.1 Aeroservoelastic Modeling

The modeling process involves the ModSiG-FMRA toolbox of the TU Berlin (TUB) [20] and the theoretical foundations from [7], [21] and [22]. The free flying flexible aircraft flight dynamics, are formulated in the mean axes reference frame. This formulation is able to describe the aircraft due to constant deformation, capturing the dynamics in relative motion as a floating body [23]. The mean axes reference frame simplifies the kinetic energy expressions, under the assumption of small displacements, avoiding inertial coupling between rigid and elastic degrees of freedom (DOF) [7]. Figure 1 shows the mean axes reference frame [24]. The aeroservoelastic model is represented by the non linear equations of motion (EOM) based on mean axes [7] and the unsteady (US) aerodynamic modeling technique from [23]. The EOM of the flexible flight dynamics are described by:

$$\dot{V}_{B^{(G)}}(t) = -\omega_{B^G}(t) \times V_{B^{(G)}}(t) + T_{B^{(G)}I}(t) G_I + \frac{1}{m} F^{ext}_{B^G}(t) \tag{1}$$

$$\dot{\omega}_{B^{(G)}}(t) = -J^{-1} \left(\omega_{B^{(G)}}(t) \times (J \omega_{B^G}(t)) \right) + J^{-1} M^{ext}_{B^{(G)}}(t) \tag{2}$$

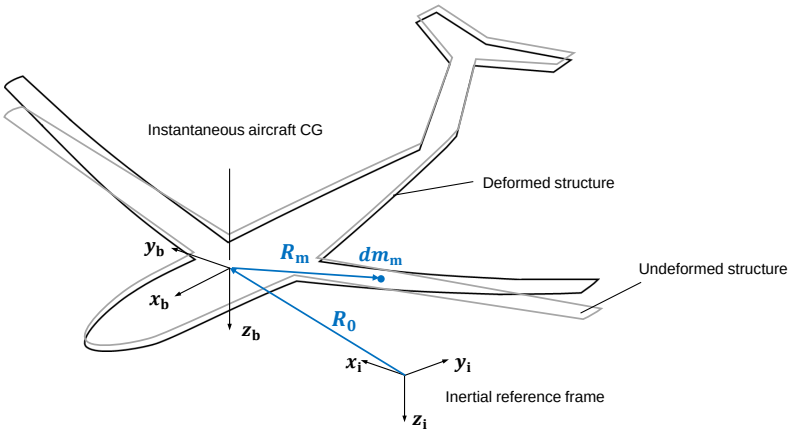

Fig. 1 Flying flexible aircraft, as well as the inertial and mean-axes' reference frames [21]

The equations of the structural dynamics are represented by:

$$\ddot{\eta}\left(t\right) = -2\xi\omega_n\dot{\eta} - \omega_n^2\eta + \mu^{-1}Q_\eta \tag{3}$$

Equations 1 and 2 express the rigid body motion described by the six equations considering the linear velocity $V_{B(G)}\left(t\right)$ and the rotational velocity $\omega_{B(G)}\left(t\right)$. The EOM for the incremental aerodynamics due to flexible deformation are denoted in the modal domain and can be expressed as in Eq. 3. The structural properties are described by the mass of the aircraft m, its inertia tensor J, generalized/modal mass μ and structural/modal damping ξ. Earth gravity is represented by G_I. The excitation of rigid and flexible dynamics of the aircraft are induced by the external forces $F_{BG}^{ext}\left(t\right)$ and moments $M_{B(G)}^{ext}$ in Eq. 1 and 2, on the right-hand side. In other words, the external forces and moments have components from the rigid body and flexible contribution, where the latter are expressed through incremental generalized loads Q_η. The incremental loads Q_η couple the EOM with the structural dynamics in Eq. 3. For load alleviation control purposes and quantification of the latter, sensors are required to recover accelerations and angular rates for example. For this purpose, distributed inertial measurement units (IMU's) are placed spanwise on the wing. These virtual measurements can be recovered by means of the modal approach as in [25]:

$$d\left(x,y,z,t\right) = \sum_{i=1}^{n} \Phi_i\left(x,y,z\right)\eta_i\left(t\right) \tag{4}$$

The applied modeling technique in this work with the theoretical foundations from [7], [21] and [22] does not consider geometrically non linear effects and is therefore valid for deflections within the linear regime.

2.2 Non Linear Aircraft Dynamics Model and ModSiG Computational Framework

The previous modeling theory applied to the reference aircraft leads to the aeroservoelastic model of the free flying flexible aircaft DLR-F25 UP Wing configuration. Therefore, two types of models are developed within the ModSiG-FMRA framework [20]:

- A fully non linear model for time domain simulation and for controller validation.

- A linearized state-space model for controller synthesis numerically derived at the corresponding trim point from the non linear model.

The non linear simulation model is developed in MATLAB/Simulink, based on the aeroservoelastic formulation described previously. The input vector of the model is described as:

$$U = [m\ x_{CG}\ \delta_e\ \delta_{ail1_r}\ \delta_{ail1_l}\ \delta_{ail2_r}\ \delta_{ail2_l}\ \delta_{oflap_r}\ \delta_{oflap_l}\ \delta_{flaperon_r}\ \delta_{flaperon_l}\ \delta_{iflap_r}\ \delta_{iflap_l}\ \delta_r\ \delta_T\ w_x\ w_y\ w_z]^T, \tag{5}$$

where m corresponds to the mass of the aircraft and x_{CG} to the respective CG position in x direction. All control surfaces of the aircraft are considered as right and left pairs of the wing as δ_{CS}, where the corresponding control surface is denoted as a subscript. The thrust input is denoted as δ_T and the wind components in each direction are considered as w. The state vector of the model is defined as:

$$X = [V\ \Theta\ H\ \alpha\ q\ \beta\ r\ \phi\ p\ \Psi\ x_e\ y_e\ \eta_i\ \dot{\eta}_i\ \lambda_{1_W}\ \lambda_{2_W}\ \lambda_{1_{HE}}\ \lambda_{2_{HE}}\ \lambda_{1_{VE}}\ \lambda_{2_{VE}}]^T \tag{6}$$

and the available outputs of the model are:

$$\begin{aligned} Y = [&V\ \Theta\ H\ \alpha\ q\ \beta\ r\ \phi\ p\ \Psi\ x_e\ y_e\ \eta_i\ \dot{\eta}_i\ \lambda_{1_W}\ \lambda_{2_W}\ \lambda_{1_{HE}}\ \lambda_{2_{HE}}\ \lambda_{1_{VE}}\ \lambda_{2_{VE}}\ \varphi_W\ \gamma_W\ \varphi_{HE}\ \gamma_{HE}\ \varphi_{VE}\ \gamma_{VE} \\ &p_W\ q_W\ r_W\ p_{HE}\ q_{HE}\ r_{HE}\ \dot{p}\ \dot{q}\ \dot{r}\ \dot{p}_W\ \dot{q}_W\ \dot{r}_W\ \dot{p}_{HE}\ \dot{q}_{HE}\ \dot{r}_{HE}\ a_{x_W}\ a_{y_W}\ a_{z_W}\ a_{x_{HE}}\ a_{y_{HE}}\ a_{z_{HE}} \\ &a_{x_{CP}}\ a_{y_{CP}}\ a_{z_{CP}}\ a_{x_{LPAX}}\ a_{y_{LPAX}}\ a_{z_{LPAX}}\ WRM_x\ WRF_z\ a_{x_{CG}}\ a_{y_{CG}}\ a_{z_{CG}}]^T, \end{aligned} \tag{7}$$

where in X, the rigid body states of the aircraft, as well as the flexible states η, their derivatives $\dot{\eta}$ and the unsteady aerodynamic lag states λ per each lifting surface are represented. In Y, additionally to the states in X, further outputs as angular velocities and accelerations p, q, r and $\dot{p}, \dot{q}, \dot{r}$ and translational accelerations a in all 3 axes are provided. These quantities are measured at different positions on the structure of the aircraft as detailed in each subscript. The quantities φ and γ correspond to the bending and torsional components as according to [23] and additionally the moment around x and the force in z direction at the wing root are computed in the output vector Y. Figure 2 shows the simplified workflow for the non linear flexible aircraft simulator with unsteady aerodynamics developed in [20], applied to the UP Wing configuration in [26] and optimized for real-time simulation in [27] by pre-calculating all time invariant flexible influence coefficients from the quasi-steady (QS) and unsteady (US) modeling formulations. The ModSiG-FMRA framework shown in Fig. 2 models the flexible aircraft dynamics using modal superposition. It requires modal data from MSC Nastran [28] (SOL103) and structural node positions for discretization and aerodynamic interpolation. This is simplified by condensing all modal properties to the load reference axis of the aircraft. Aerodynamics for the incremental loads due to deformation is modeled via strip theory, while engine thrust and geometry are predefined. Trim conditions are solved in MATLAB with the routine *fsolve* and the system is numerically linearized to derive state-space matrices (A, B, C, D). Simulations are executed in Simulink using S-functions.

2.3 Linear Model for Controller Design

The linear state-space model for controller synthesis is derived from the non linear model and has the following mathematical representation:

$$\begin{aligned} \dot{x} &= A\ x + B\ u \\ y &= C\ x + D\ u \end{aligned} \tag{8}$$

For this procedure, the non linear model is trimmed at an altitude of $H = 6000\ m$ and at a Mach number of 0.78, which is equivalent to an indicated airspeed of $V = 246.81\ m/s$. The aircraft is then numerically linearized around this condition. The inputs, states and outputs are equal for the non linear, as well as for the linear model. Both systems have a total of 240 states.

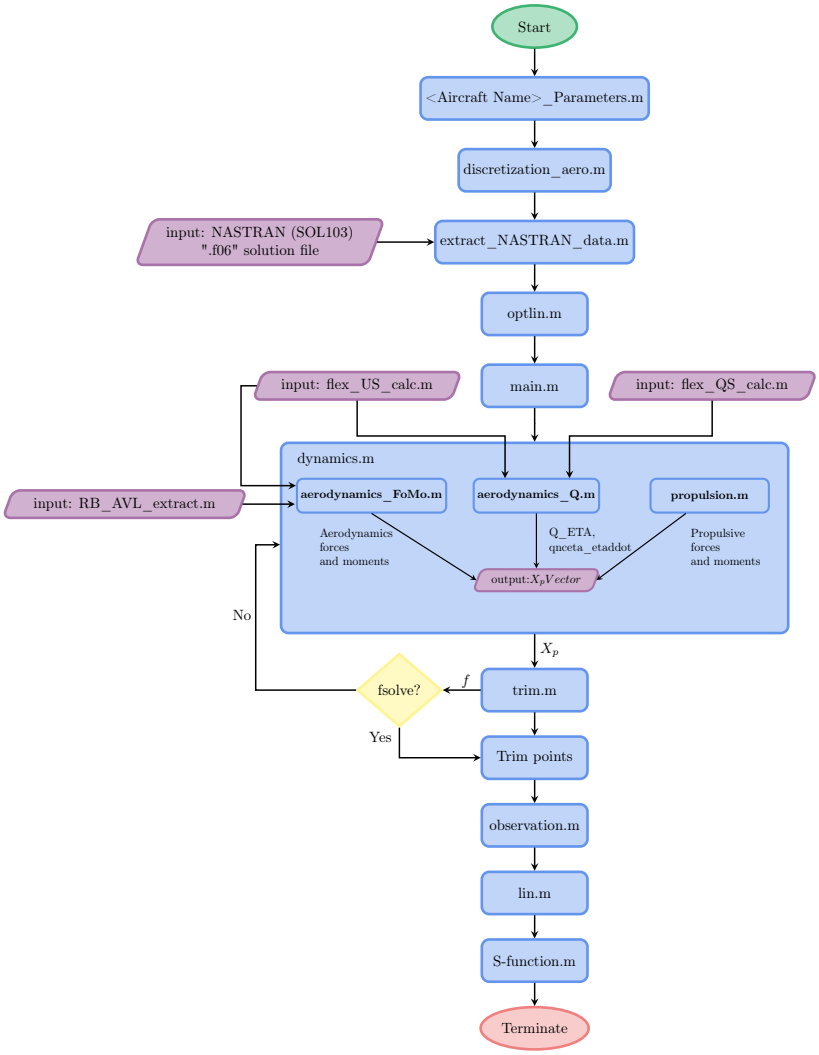

Fig. 2 Simplified flow chart of the flexible simulator with US aerodynamics [26]

2.4 Comparison to Higher Complexity Methods

To derive meaningful control laws a numerical validation in time and frequency domain is performed against the higher complexity simulation environment UltraFLoads [19], as detailed in [29]. UltraFLoads incorporates DLR's CFD code Tau with linear structural dynamics and non linear flight dynamics. This enables the representation of all aerodynamic non linearities like shock-motion and flow separation in time domain. Figure 3 shows a time domain simulation of the longitudinal flight dynamics for the cruise case as a comparison between the low order ModSiG framework and the higher complexity CFD environment for a doublet input on the elevator. A numerical validation in time and frequency domain is conducted in [29] leading to a reasonable representation of the flexible aircraft dynamics at the expense of a fraction of the computational cost compared to the higher complexity environment UltraFLoads. Table 2 shows an example of the computational effort required for open loop simulations.

Table 2 Computational cost between low-order modeling technique and CFD simulation (run on 512 cores on DLR's HPC cluster CARO)[29]

	ModSiG Non Linear Model	CFD
Simulation time	5.5 s	5.5 s
Wall clock time	8.3 s	≈ 44 h

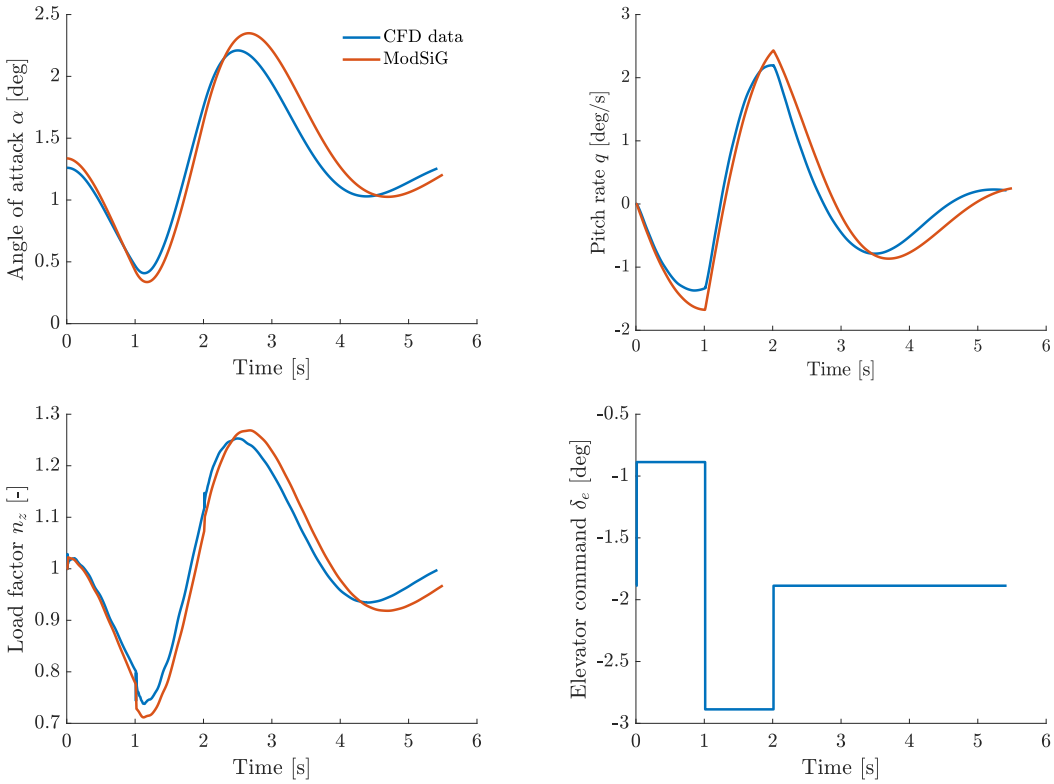

Fig. 3 Comparison between higher complexity CFD simulation and non linear ModSiG framework for a 0.5 Hz elevator doublet input at cruise conditions

3 Longitudinal Load Alleviation Control

The control law design for the free flying flexible aircraft must consider flight dynamics and structural flexibility in order to ensure proper flying qualities for a real transport aircraft. First, an autopilot including a base controller for longitudinal dynamics is developed in Section 3.1. After this, a GLA controller is synthesized based on this closed loop plant to alleviate the loads acting on the wing in Section 3.2. The requirements for the control law design in longitudinal motion are detailed in Section 3.3.

3.1 Longitudinal Autopilot and Base Controller for Flight Dynamics

The controller design is based on eigenstructure assignment, by placing the closed loop eigenvalues and explicitly assigning the eigenvectors. This technique is advantageous for decoupling controllers in MIMO systems, to ensure that only the predefined inputs influence the proposed outputs. Therefore, the rigid body eigenmodes of the aircraft are assigned by eigenstructure assignment to enforce suitable specifications for the flying qualities according to [30], [31] and [32]. The base controller for flight mechanics in longitudinal motion is derived as in [33] and [34]. Section 3.3 details the exact specifications for the longitudinal controller. The eigenvectors are specified such that the velocity and the altitude are decoupled for longitudinal motion and proper flying qualities for the rigid body dynamics are met.

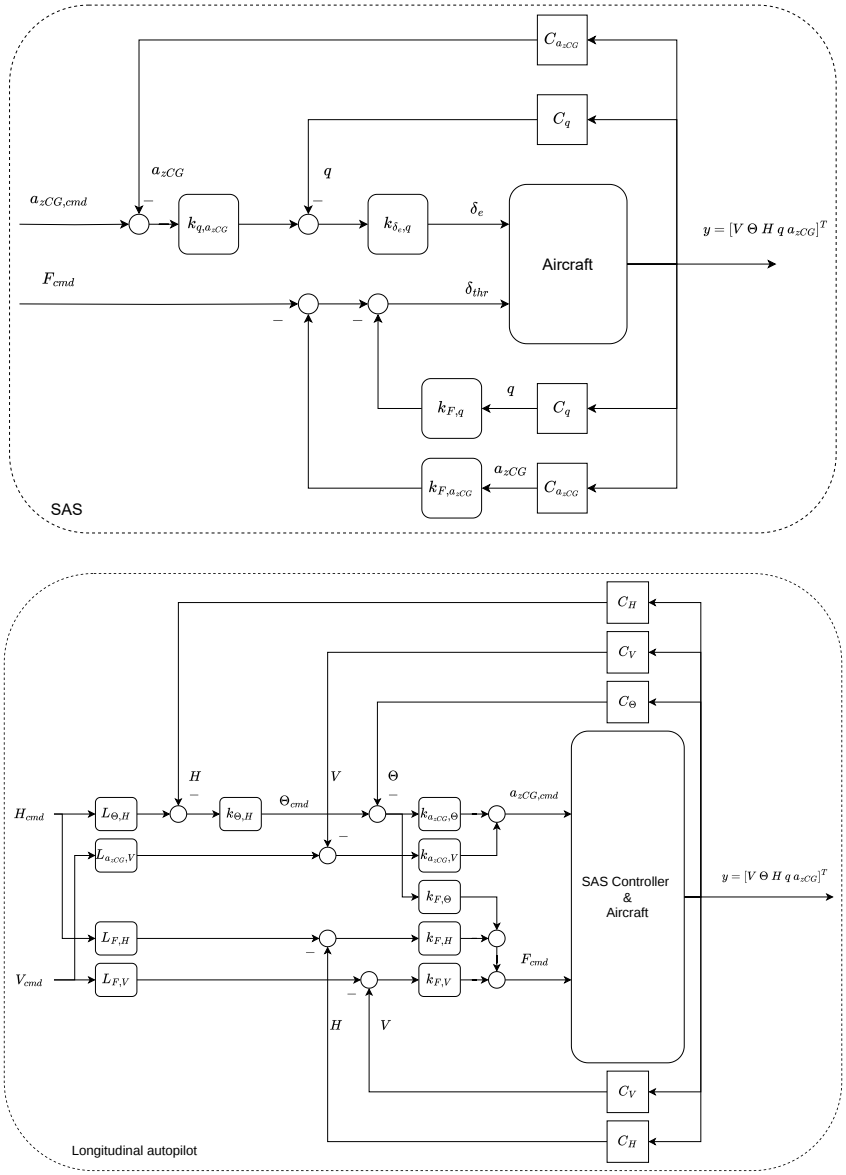

Fig. 4 Inner control loop structure SAS developed as in [34] and CAS (base controller) as well as autopilot developed as in [33]

Then, the resulting control law is applied to the reduced longitudinal plant as in [33]:

$$\begin{aligned} \dot{x}_{lon} &= A_{lon}\, x_{lon} + B_{lon}\, u_{lon} \\ y_{lon} &= C_{lon}\, x_{lon} + D_{lon}\, u_{lon} \end{aligned} \tag{9}$$

Since the reduced system for the longitudinal motion (rigid body) shows 5 independent states, the state-space structure allows full state feedback with the following control law:

$$\begin{aligned} u &= -K_y\, y + L\, r \\ \text{with } r &= [V_{ref}\ H_{ref}]^T \end{aligned} \tag{10}$$

This control law includes a SAS, a CAS, with the latter serving as the base controller, and a longitudinal autopilot enabling the tracking of velocity and altitude. The diagrams in Fig. 4 shows the longitudinal SAS, CAS and autopilot. As shown above for the SAS the pitch rate q and acceleration in z-direction on the CG $a_{z_{CG}}$ are fed back to the elevator and thrust input. In the diagram shown below, the SAS

is already represented within the block "SAS Controller & Aircraft" yielding a total of 10 feedback gains. Furthermore, within the control synthesis process, 4 filters are designed: $L_{\Theta,H}$, $L_{a_{zCG},V}$, $L_{F,H}$ and $L_{F,V}$ to guarantee optimal stationary guidance accuracy for both reference inputs in velocity and altitude $\left[V_{ref}\ H_{ref}\right]^T$.

3.2 Gust Load Alleviation Controller

The proposed control law synthesis procedure is the LQR output feedback method [18] [35]. This control law is synthesized on the closed loop plant for the longitudinal autopilot. Figure 5 shows the GLA controller as an outer loop structure considering the longitudinal autopilot, which includes the SAS and CAS (base controller). The LQR output feedback method can be applied to state-space models as

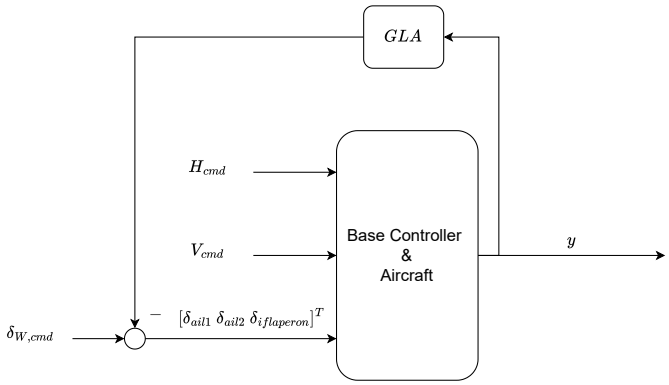

Fig. 5 Longitudinal GLA controller structure

in Eq. 9. For the controller action $u = -Ky$ applies. To alleviate structural loads, only the WRBM and WRTF are weighted in the performance index J by modifying the matrix Q_{mod}. The available measurements C_{meas} are considered for the corresponding feedback gain K within the control energy term of the performance index J. The controller gain K is then computed by minimizing the performance index J:

$$Q_{mod} = C_{mod}^T \cdot I \cdot C_{mod} \tag{11}$$

$$J = \frac{1}{2} \int_0^\infty x^T (Q_{mod} + C_{meas}^T K^T R K C_{meas}) x \, dt \tag{12}$$

The optimization is accomplished with MATLAB's function *fmincon* to compute a minimum of a non linear multivariable function subject to constraints. An outcome of the solution, commonly known among minimization problems, is that there is a risk to convergence to local minima. Nevertheless, since the final closed loop performance is considered the crucial measure for the design, a possible locally optimal solution is acceptable as long as the performance requirements are satisfied [36]. In order to mitigate this matter and to improve the proper assessment of a given feedback structure, the weightings of WRBM and WRTF are additionally varied logarithmically from 10^{-11} to 10^{-6}, for the specific case of the control law presented in Eq. 13. Therefore, different controllers are synthesized by multiplying Q_{mod} with 10^{-11} to 10^{-6}, resulting in a controller spectrum for a given feedback structure. These values result in order to find an equilibrium point between the output weighting Q_{mod} and the control energy considered in $C_{meas}^T K^T R K C_{meas}$, such that both terms are in a similar order of magnitude. This controller spectrum is assessed in terms of WRBM reduction and required actuator deflection. This methodology is applied to different feedback structures, adjusting the feedback controller matrix K, to explore the best suitable

feedback layout. One feasible control law example using accelerations in z-direction a_z is:

$$\begin{bmatrix} \delta_{ail2l} \\ \delta_{ail1l} \\ \delta_{iflaperonl} \\ \delta_{iflaperonr} \\ \delta_{ail1r} \\ \delta_{ail2r} \end{bmatrix} = - \begin{bmatrix} K_1 & 0 \\ K_1 & 0 \\ K_2 & 0 \\ 0 & K_2 \\ 0 & K_1 \\ 0 & K_1 \end{bmatrix} \begin{bmatrix} a_{z5} \\ a_{z8} \end{bmatrix} \tag{13}$$

The given control law is a consequence of an iterative control design process to first, meet all requirements and second, achieve the best possible performance in non linear simulations in the low-order simulation framework, as well as in the higher complexity environment. Within this process the described methodology is applied first considering all available measurements for feedback to all available control surfaces for GLA. According to the assessment the dimension and complexity of the controller gain K is reduced iteratively since for this case the robustness margins and the actuator limitations are the most challenging constraints to fulfill. A step by step reduction of the controller dimension leads to a feasible controller as in Eq. 13, which is able to comply with all requirements. Within the control synthesis, actuator dynamics as described in Section 4.3 are considered. Time delay is also considered as a second order Padé approximation for the GLA feedback controller.

3.3 Control law design requirements

For the control law design in longitudinal motion, the following requirements are considered:

- Phugoid: Target a damping of 0.4, according to MIL-STD-1797 [32] and MIL-F-8785C [37].
- Short-Period: Target a damping of 0.4 and a frequency of 2.0 rad/s, according to MIL-STD-1797 [32] and MIL-F-8785C [37].
- Robustness margins: Maintain a phase margin of 30° and gain margin of 6 dB, as recommended in flight control practices [38].
- Time delay: Robust against time delay in control servo loop by at least 60 ms [39].
- Actuator limitations: Maximum deflections of ±15° and angular velocities of $\pm 50 \frac{°}{s}$ [40].
- Actuator cut-off frequencies: Conservatively defined as in [13], with WISDOM project findings suggesting future cut-off frequencies between 6–7 Hz [33].
- Performance in WRBM reduction: Minimum 10% reduction to achieve significant weight savings.

The control law shown in Eq. 13 satisfies the given requirements, whereas different control laws can be synthesized with the proposed methodology.

4 Study Case High-Aspect Ratio DLR-F25 UP Wing Configuration

The aircraft developed within the federal aviation research program VirEnfREI [15] is investigated in several projects with different variations for specific purposes, whereas for UP Wing adaptations of the wing airfoils were performed as in [41]. The work conducted in this investigation is applied to the baseline configuration of the DLR-F25 shown in Fig. 6. Table 3 shows the global properties of the DLR-F25 version used as the reference aircraft for this investigation. The conditions and mass case chosen, represent the most critical gust load case as according to higher complexity simulations from [41], which is why this specific condition and mass case are analyzed.

4.1 Structural Modeling

The structural properties are represented by Eq. 3 in the modal domain mainly by the modal mass and modal damping matrices. These are obtained from a FE model using MSC Nastran [28] SOL 103,

Fig. 6 Global FE model of the DLR-F25 UP Wing [15] and DLR-F25 configuration: Outer shape and structural components [41]

Table 3 Global properties of the UP Wing model DLR-F25 MTOW configuration [41]

Global properties	
Wing span	45 m
Wing area	130.1 m^2
Aspect ratio	15.6
Mass	85954.11 kg
Mach number	0.78
Initial altitude	6000 m

which provides a modal analysis (.f06 file). For simplification, the FE model has a load reference axis, where the structural properties are condensed, leading to a beam representation [42], which is predefined in the DLR modeling process. Since all modal properties are transferred to this axis, they can be directly extracted, avoiding otherwise labor intensive interpolation of structural nodes. The number of considered modes can be predefined when linearizing the non linear model around a trim condition. Already 20 modes up to 15 Hz have been found to accurately represent the flexible dynamics of the aircraft [29] [43], with the first structural mode at 2.28 Hz. Modes beyond 15 Hz are considered difficult to control due to actuator limitations. Since the modal analysis reveal important characteristics about the flexible behavior of the aircraft and has a direct influence in the modeling process, a brief overview of the eigenmodes is presented in Table 5 (Appendix). The modal properties are representative for the MTOW mass case with distributed wing mass and the global properties from Table 3.

4.2 Rigid Body Flight Dynamics Model and Aerodynamic Modeling

The rigid body flight dynamics model is developed with Athena Vortex Lattice (AVL) which is a Vortex Lattice Method (VLM) software [44]. In this approach an aerodynamic distribution correction is included from CFD data. The aircraft is represented by bound vortices, allowing AVL to compute aerodynamic forces, moments, and spanwise distributions for a specific flight condition. Stability and control surface derivatives are extracted to assemble the model, with layouts and wing profiles defined as in [1]. Figure 7 shows the developed AVL model. In this regard the CFD data consider the aircraft as a flexible body whereas AVL represent the aircraft as a rigid body. AVL includes compressibility corrections for higher Mach numbers, but further accuracy is achieved by replacing AVL's distributed aerodynamics (without control surface derivatives) with CFD lift and drag slope data. Figure 7 compares both, showing the significant difference between transonic (CFD) and subsonic (AVL) distributions. The principal factors affecting accuracy are the wing twist and camber distributions from the jig shape in the FE model, captured through section profile coordinates, which directly influence stability derivative computation. In

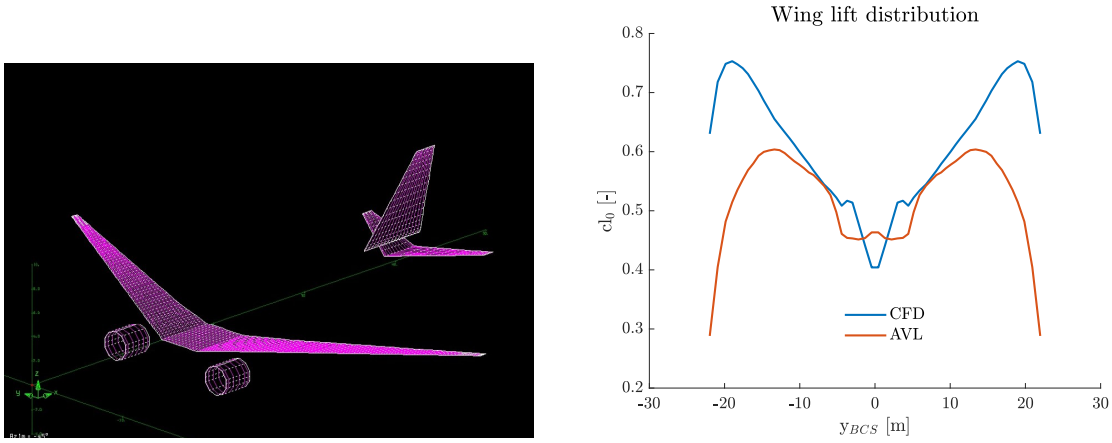

Fig. 7 Rigid body AVL model of the UP Wing DLR-F25 baseline aircraft and Wing lift distribution for $\alpha = 0°$

total, the following corrections are applied during the modeling process to take into account the transonic aerodynamics. Firstly, the Prandtl-Glauert compressibility correction is used in AVL. Secondly, not the reference Mach number is used for the stability derivatives computations, but instead the corrected Mach number perpendicular to the quarter chord line of the wing: $M_{corr} = M \cdot cos(\Lambda)$, here $\Lambda = 27.4°$ is the sweep angle of the aircraft. Thirdly, for the calculation of the incremental aerodynamics due to flexible deformation the distributed aerodynamic slopes C_{L_α}, C_{D_α}, C_{L_0} and C_{D_0} from CFD computations are used. These are incorporated into the formulation of the QS and US aerodynamic modeling techniques, when calculating the incremental QS [22] and US [23] aerodynamic coefficients due to flexible deformation. Lastly, for this study, with a focus on longitudinal motion and additionally improved modeling accuracy, the stability derivatives associated with longitudinal dynamics are corrected using CFD derived stability derivatives. The corrected stability derivatives are: C_{L_0}, C_{L_α}, C_{L_q}, $C_{L_{\delta e}}$, C_{m_0}, C_{m_α}, C_{m_q} and $C_{m_{\delta e}}$.

4.3 Actuator and Sensor Modeling

The control surfaces are modeled within AVL, where the control surface derivatives and control surface lift slopes are extracted in a first step, based on the geometry defined in the CPACS data from [1] [40]. Figure 8 visualizes the DLR-F25 wing layout. The control surface derivatives distributions are complemented with higher complexity data from CFD to refine the control surface efficiency. CFD data including the derivative distributions of each control surface available for GLA are included by calculating the incremental QS aerodynamic coefficients due to flexible deformation from the QS formulation [22]. Since deflections are limited by actuator dynamics, each control surface is represented by a first order linear time-invariant actuator model as in [40] and integrated into the aeroservoelastic plant. Specifications follow [33], with a 6 Hz actuator cut-off frequency, maximum flaperon deflections of ±15°, and angular rates of $\pm 50°/s$ [40]. Virtual IMU sensors are installed to provide accelerations (a_x, a_y, a_z) and angular rates $(p_{IMU}, q_{IMU}, r_{IMU})$ measurements for feedback control. They are positioned on the load reference axis of the wing, HE, cockpit, and last PAX locations. To capture structural modes, 12 sensors are distributed approximately every 20% along the wing half-span, and 4 are placed on the HE, as shown in Fig. 9.

4.4 Gust Model

Critical wind gusts can excite the aircraft structure and induce stresses on wing, fuselage, and tailplane. To ensure structural integrity and meet certification standards CS-25 [30], simulations of gust loads must be performed, accounting for aeroelastic response from structural dynamics and unsteady aerodynamics. CS-25, article 25.341, specifies two excitation types: discrete gusts, defined by amplitude

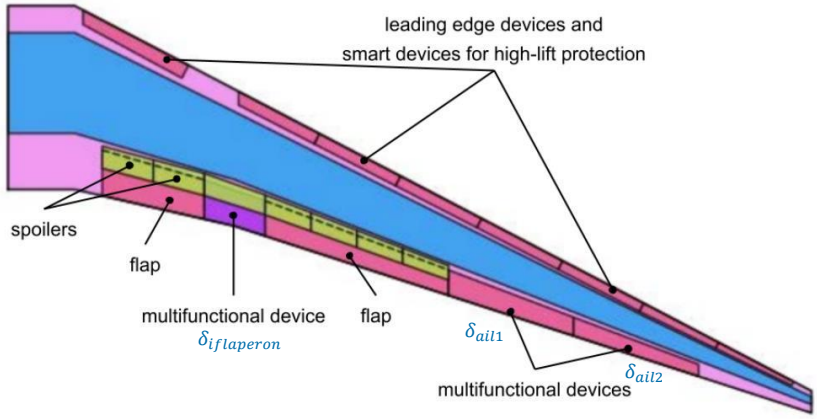

Fig. 8 Wing movable layout concept defined for UP Wing configuration [1]

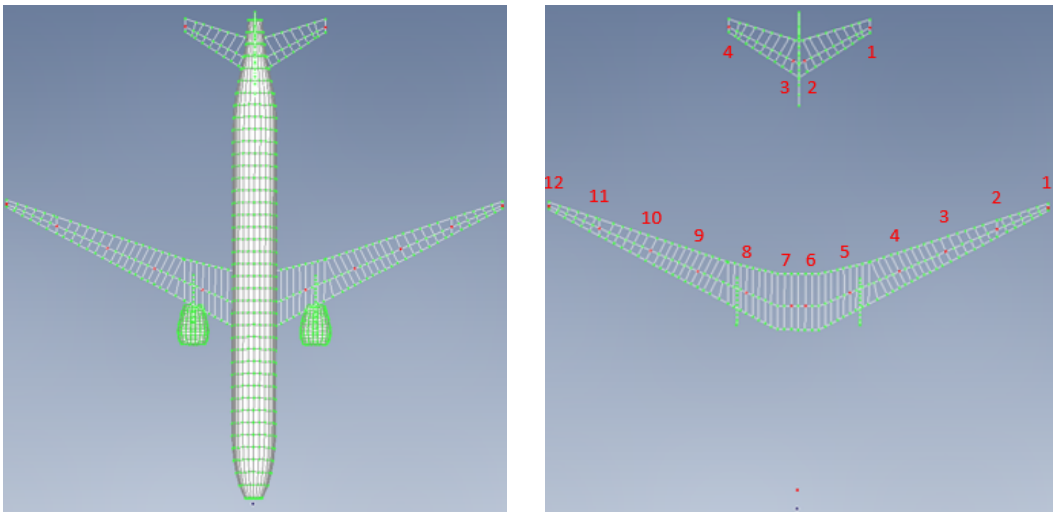

Fig. 9 Location of the sensors distributed over the wing, HE, cockpit and last PAX position visualized in FEMAP

and gradient length and equivalent to single-frequency perturbations, and continuous turbulence, which excites a frequency range. The vertical 1-cosine discrete gust is expressed in the time domain as [13]:

$$v_z(t) = \begin{cases} \frac{U_{\text{gust}}}{2}\left[1 - \cos\left(\frac{\pi t V}{L_{\text{gust}}}\right)\right] & \text{if } 0 \le t \le \frac{2L_{\text{gust}}}{V} \\ 0 & \text{otherwise} \end{cases} \tag{14}$$

In this expression, t is time (s), V true airspeed (m/s), L_{gust} the gust gradient (ft), and U_{gust} the gust amplitude (m/s), which depends on L_{gust} and further flight parameters [30]:

$$U_{\text{gust}} = U_{\text{ref}} \cdot F_g \cdot \left(\frac{L_{gust}}{350\ \text{ft}}\right)^{1/6} \tag{15}$$

Generally, gradients range from 30–350 ft, producing different frequency excitations. Shorter gusts yield smaller amplitudes but higher frequencies, which are more difficult to attenuate due to actuator bandwidth limitations [13]. In this work, only the rigid body excitation of the gust acting on the aircraft CG is considered.

5 Results

The longitudinal autopilot controller structure presented in Fig. 4 allows tracking altitude and velocity, and the GLA controller structure shown in Fig. 5 reduces the loads on the wing structure, by commanding in longitudinal motion the available wing control surfaces symmetrically. For load alleviation there are three control surfaces available: the inner flaperon and both outer flaperons. Those are defined as in Fig. 8 as the inner multifunctional device and both outer multifunctional devices. The mentioned 3 control surfaces are equivalent to $\delta_{flaperon}$, δ_{ail1} and δ_{ail2} in the state-space model.

5.1 Stability Analysis and MAC Criteron

The rigid body eigenmodes in longitudinal motion become real poles due to the tracking capability derived from the eigenstructure assignment procedure, and therefore the poles develop a first order behavior resulting in a damping ratio equal to 1. This is also depicted in Fig. 10. The global and rigid body

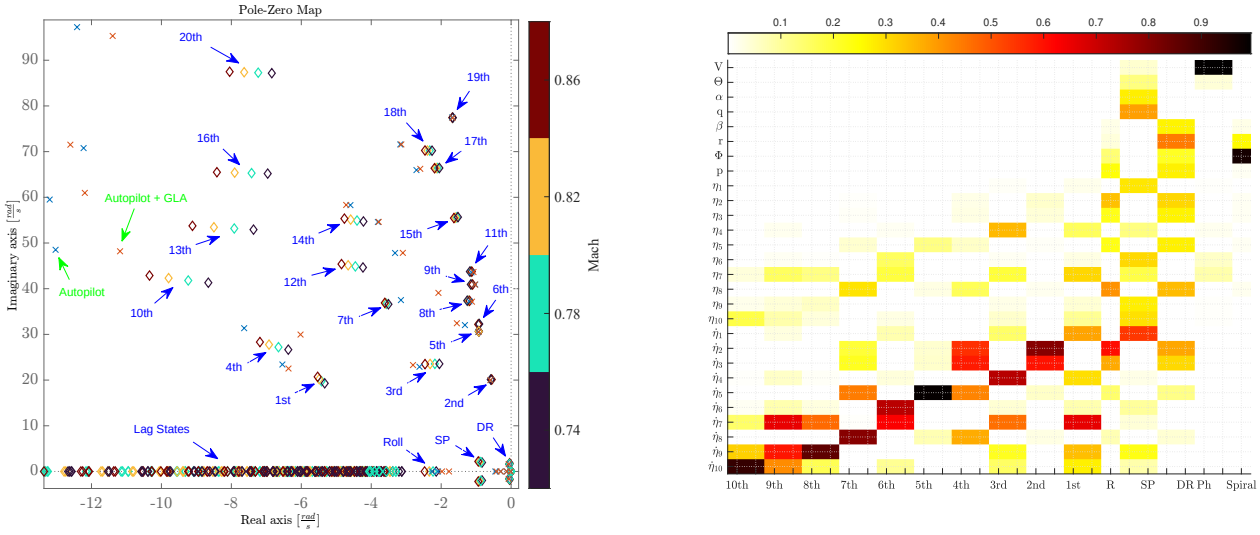

Fig. 10 Global pole zero maps for open loop response for a Mach variation and closed loop behavior for Mach 0.78 and MAC map of the DLR-F25

pole zero map for open loop response and a variation of the Mach number from 0.74 to 0.86, presented by the diamond markers, are shown in Fig. 10. The light blue crosses show the autopilot and the red crosses show the autopilot with GLA controller using translational accelerations as feedback sensors. Important to notice is that the closed loop systems are presented as reduced order models (ROMs), because both closed loop systems are synthesized on the ROMs. The open loop systems are presented as FOMs. A total of 20 flexible modes are described together with the rigid body eigenmodes.

Figure 10 also shows the Modal Assurance Criterion (MAC) map of the DLR-F25 UP Wing configuration. This MAC visualization shows the extent in consistency between a normalized mode and the states of the considered system. As a consequence, a MAC value heading towards 1 is an indication that the normalized mode is highly related to a certain state of the system. On the other hand, a low value around 0 means that low correlation between normalized modes and states are present [20]. The MAC map shown in Fig. 10 is derived for the conditions from Table 3. On the y-axis the states of the system are presented considering the rigid body states and the first 10 modal shapes and their derivatives. On the x-axis the rigid body modes as well as the first 10 structural modes are depicted. The MAC map and the corresponding correlation value shows the interaction between the rigid body modes and the structural modes. In detail in Fig. 10, the Phugoid mode is mainly coupled with the longitudinal states V and Θ. The Short Period mode is coupled to the longitudinal states q, α, Θ and in less extent to V. In this

mode also a contribution from the modal shapes η_1, η_4, η_6, η_7, η_9 and η_{10}, as well as their modal shape derivatives is present. All of them correspond to wing or fuselage symmetrical contributions, where among them η_1 and $\dot{\eta}_1$ have the strongest contribution together with q to the Short Period mode. This analysis exposes important coupling mechanism especially for high-aspect ratio wing flexible aircraft, such as the DLR-F25, emphasizing the interaction between the flight dynamic modes (Short Period mode) and structural modes (1st symmetric wing bending mode).

5.2 Robustness Analysis

Figure 11 shows the bode diagram of the open- and the closed loop response. The open loop response is represented by the transfer function from the elevator δ_e to the pitch rate q at the CG. The closed loop responses are described by the autopilot command from altitude H_{cmd} to the pitch rate q at the CG. For the open loop response, the Phugoid and the Short Period mode can be located at a frequency of 0.059 rad/s and 2.22 rad/s respectively. For the closed loop response the bode diagram represents the attenuation of both longitudinal rigid body eigenmodes and notable attenuation of further aeroelastic response in the higher frequency regime. This is reasonable, since the autopilot is responsible for the rigid body eigenmodes to emerge as real poles, removing any rigid body eigenmode dynamics in longitudinal motion. Figure 11 also shows the Multiple-Input-Multiple-Output (MIMO) stability margins of the closed

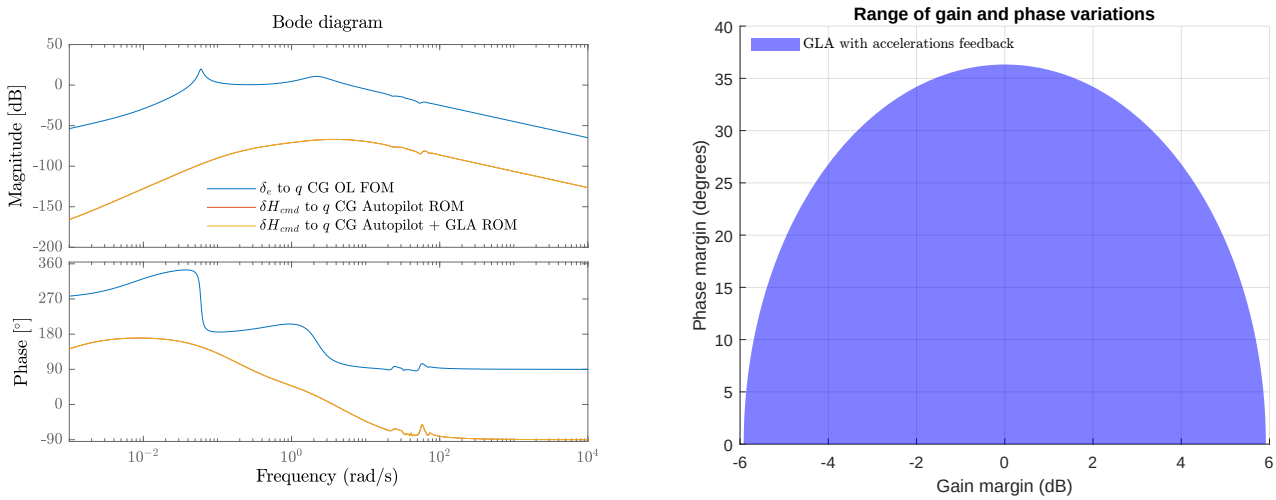

Fig. 11 Open and closed loop bode diagram for Mach = 0.78 and Disk-based stability margins for the GLA controller

loop system at the input. The GLA controller with feedback of translational accelerations is analyzed in this regard. The reduced order models are considered for this analysis. Only the feedback loop of the GLA controller to the augmented plant (autopilot and flexible aircraft) is analyzed and therefore no robustness assessment respecting the autopilot is provided. Detailed description of the location of the sensors and which control surfaces are actuated are given in sections 3.2 and 4.3. The GLA controller with translational accelerations feedback is able to comply with the established stability margin requirements reaching 36.32° in phase and 5.91 dB in gain. This is achieved by a manual assessment and tuning of the controller gains by -59 % to fulfill the design requirements. The resulting trade-off between robustness and performance leads to a reduction in nominal performance to comply with increased robustness. Nevertheless, it is important to outline that the given analysis provides a conservative approach to asses the margins, since this technique considers independent and simultaneous variations at the input of the entire feedback loop [38].

5.3 Load Alleviation with LQR Output Feedback Time Domain Non Linear Simulation Results

The developed autopilot and GLA controller are integrated into the non linear simulation framework from [20] and the simulation results are shown in Fig. 12. For the simulation a 1-cos discrete gust as modeled in section 4.4 is applied to the non linear model, representing a sudden gust encounter. The parameters used in Table 4 are considered for the gust encounter, as well as for the non linear simulation. For the results shown in Fig. 12 a feedback control structure is chosen as in Eq. 13,

Table 4 Gust and simulation parameters

Parameter	Symbol	Value
Mach number	M	0.78
Altitude	H	6000 m
Actuators cut-off frequency	ω_0	6 Hz
Maximum deflection angle	u_{max}	$\pm 15°$
Maximum deflection rate	$\dot{u}_{max}$	$\pm 50 \frac{°}{s}$
Time delay	τ_{sens}	60 ms
Interpolated reference velocity	U_{ref}	12.68 $\frac{m}{s}$
Flight profile alleviation factor	F_g	0.923
Discrete gust gradient	L_{gust}	150 ft
Resulting gust frequency	ω_{gust}	2.81 Hz

using translational acceleration measurements from virtual IMUs. The sensors (highlighted in red) are located as in Fig. 9, meaning that both sensors located approximately at the engine position measure the acceleration in z-direction on the wing structure. These measurements are provided via the designed proportional controller gain K_1 to both ailerons δ_{ail1} and δ_{ail2}, meaning that they deflect equally. The same measurements are also provided to the flaperon $\delta_{flaperon}$ via the designed proportional gain K_2.

Figure 12 visualizes the comparison between the open loop response, the autopilot and GLA controller, showing notable differences between both controllers and the open loop response. The autopilot has no authority respecting the control surfaces of the wing, because no feedback loop is applied here, and therefore only the control surface deflections from the GLA controller are visualized. Since the autopilot is designed to control the flight dynamics of the aircraft and the GLA controller to attenuate the loads acting on the wing, only limited interaction between both controllers is present. This can be evaluated by examining the angle of attack, the pitch rate, the elevator and thrust commands. All of them do not differ at the first instance of the perturbation, only after the excitation, the damping is increased for the angle of attack, the pitch rate and the wing tip deformation. When examining the elevator command after the initial perturbation, a decreased control action can be observed there, since the GLA controller is also deflecting the control surfaces on the wing upwards (negatively upwards according to BCS from flight mechanics), leading to less required elevator action.

While the GLA controller deflects upwards the control surfaces on the wing, the local lift is reduced and therefore also the loads acting on the wing as visualized in the WRBM figure. The GLA controller is able to achieve up to 11.88 % in WRBM reduction compared to the open loop response. Additionally, a considerable increase in damping with respect to the open loop response is achieved. The simulation results demonstrate that incorporating a GLA controller alongside an autopilot provides significantly greater benefits in WRBM reduction compared to relying only on the autopilot itself. This is evidenced in the behavior of the WRBM. While the autopilot alone increases overall damping, it is not capable

of mitigating sufficiently the initial WRBM peak, which is critical since this is where the maximum structural loads develop.

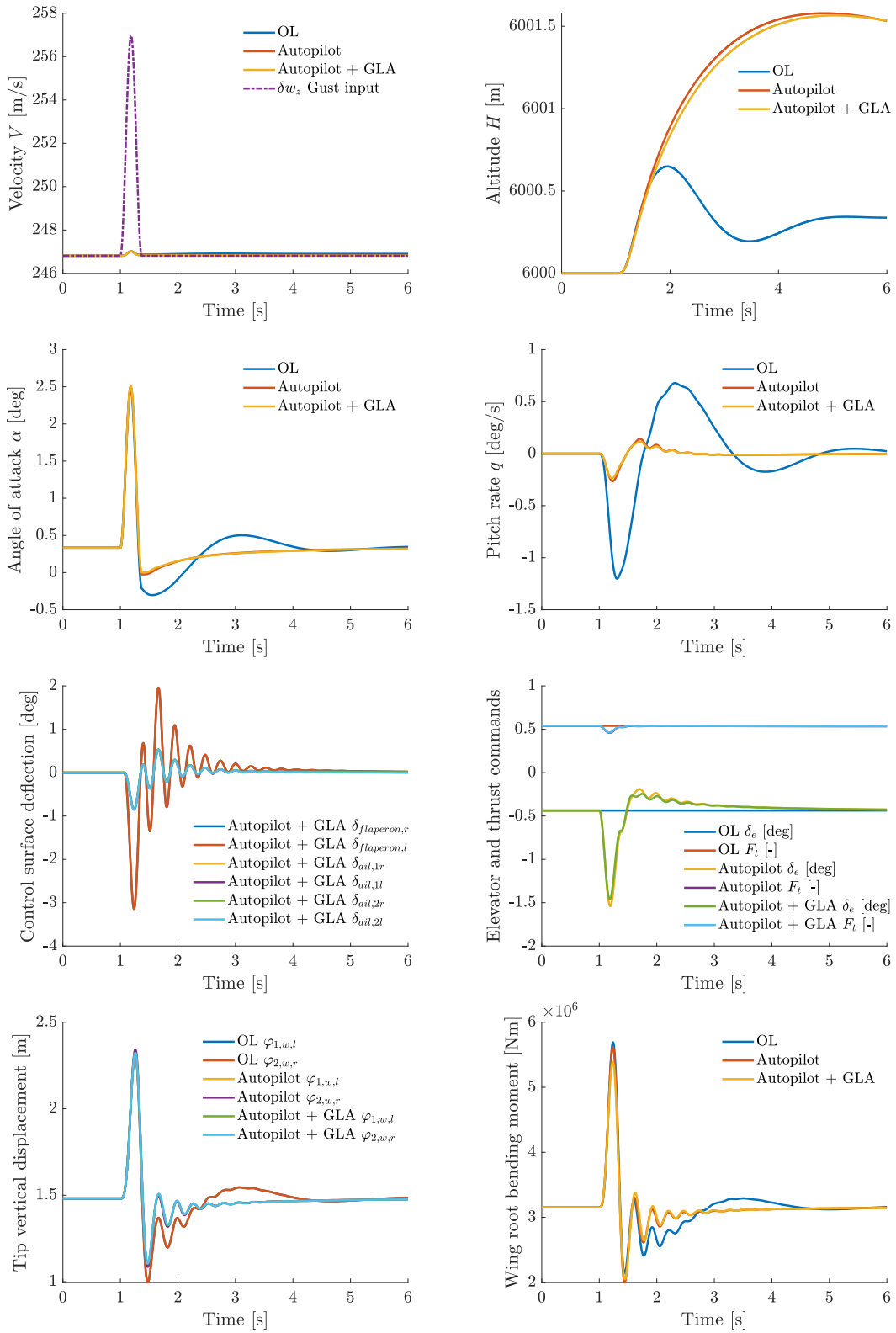

Fig. 12 DLR-F25 UP Wing configuration non linear response with translational accelerations as feedback sensors and a gust gradient of 150 ft at the CG

The proposed GLA feedback controller structure is able to provide a substantial reduction in WRBM, which can be translated into potential mass savings. At first instance, the chosen feedback structure is

investigated since IMU sensors present common solutions for real flight test control applications, due to their reliability. Nevertheless, the approach to find the best suitable controller, or the application of different control methodologies is still scope of ongoing investigation.

6 Conclusion

This paper provides a framework for a straightforward active longitudinal load control methodology applied to the high-aspect ratio wing flexible aircraft DLR-F25 with an aspect ratio of 15.6. This methodology is successfully divided into 2 dedicated tasks. The autopilot for flight dynamics is able to stabilize the aircraft and to track velocity and altitude. The GLA control law derived, targeting the WRBM and WRTF in the control synthesis by dedicated modification of the performance index, is capable of achieving 11.88 % in load alleviation, using acceleration sensors as feedback sensors, compared to the open loop response. The GLA synthesis procedure offers the capability to parametrically assess a given feedback structure considering a variation of the penalization of the performance index. This is evaluated in terms of required control surface deflection and WRBM reduction. Due to its simplicity, this framework is suitable for embedment into higher complexity simulation environments or real flight test applications. The presented GLA controller is able to fulfill the established robustness requirements that conservatively consider multi-loop and simultaneous variations at the input. Furthermore, the simulation results show the advantage of including a GLA control loop aligned together with an longitudinal autopilot, highlighting the substantial benefit of the GLA controller that is able to reduce the first peak of the WRBM. Although the autopilot alone increases overall damping, it is not able to achieve a significant reduction of the first peak. Despite the fact that the results show the capability of what can be achieved in terms of load alleviation, different approaches can be applied regarding optimal feedback sensors and different control synthesis methods. Therefore, further controller strategy investigations are scope of ongoing investigation. The developed control laws are prepared for further integration into higher complexity simulation environments such as UltraFLoads, enabling closed loop low-order simulation results as a primary assessment tool for closed loop higher complexity simulation results.

Appendix

Table 5 First 20 eigenvalues of the UP Wing structural model DLR-F25 MTOW configuration

Mode	Frequency f, [Hz]	Description
1	2.28	1st symmetric wing bending
2	3.03	1st asymmetric wing bending + engine out-of-plane motion + fuselage in-plane bending + vertical tail in-plane bending
3	3.46	1st asymmetric wing bending + engine out-of-plane motion + vertical tail in-plane bending
4	3.65	2nd symmetric wing bending + 1st fuselage out-of-plane bending
5	4.88	Wing in-plane asymmetric motion + 2nd symmetric wing bending + engine in-plane motion
6	5.14	Engine out-of-plane motion + 1st wing torsion + fuselage out-of-plane bending
7	5.61	3rd symmetric wing bending + wing in-plane symmetric motion + engine out-of-plane motion
8	5.64	2nd asymmetric wing bending + engine out-of-plane motion
9	6.14	3rd symmetric wing bending + wing in-plane symmetric motion
10	6.61	Wing in-plane symmetric motion + 3rd symmetric wing bending
11	6.67	Horizontal tail asymmetric bending + small 2nd asymmetric wing bending
12	7.05	Engine in-plane motion + horizontal tail asymmetric bending + wing in-plane asymmetric motion
13	8.04	3rd asymmetric wing bending + horizontal tail asymmetric bending
14	8.38	Horizontal tail symmetric bending
15	8.95	Vertical tail bending + horizontal tail asymmetric bending
16	10.10	4th symmetric wing bending
17	10.55	4th asymmetric wing bending + vertical tail bending + horizontal tail in-plane bending
18	11.14	Horizontal tail symmetric bending + 2nd fuselage out-of-plane bending
19	12.31	Wing in-plane asymmetric motion + horizontal tail in-plane motion
20	13.63	5th asymmetric wing bending

Acknowledgments

The project Ultra Performance Wing (UP Wing, project number: 101101974) is supported by the Clean Aviation Joint Undertaking and its members. Co-Funded by the European Union. Views and opinions expressed are however those of the author(s) only and do not necessarily reflect those of the European Union or Clean Aviation Joint Undertaking. Neither the European Union nor the granting authority can be held responsible for them.

Declaration of Use of Artificial Intelligence

Artificial intelligence was used only to compress certain parts of the text for improved readability.

References

[1] B. Stefes A. Eberle and D. Reckzeh. Clean Aviation Ultra-Performance Wing (UP Wing). *AIAA Scitech 2024 Forum*, 2024. doi: 10.2514/6.2024-2109.

[2] Thomas E Noll, John M Brown, Marla E Perez-Davis, Stephen D Ishmael, Geary C Tiffany, and Matthew Gaier. Investigation of the helios prototype aircraft mishap volume i mishap report. *Downloaded on*, 9:2004, 2004.

[3] Carlos ES Cesnik, Patrick J Senatore, Weihua Su, Ella M Atkins, and Christopher M Shearer. X-hale: A very flexible unmanned aerial vehicle for nonlinear aeroelastic tests. *AIAA journal*, 50(12):2820–2833, 2012.

[4] Mayuresh J Patil and Dewey H Hodges. Flight dynamics of highly flexible flying wings. *Journal of Aircraft*, 43(6):1790–1799, 2006. doi: 10.2514/1.17640.

[5] CAJU. Ultra Performance Wing, 2022. Last review on 08.12.2022. `https://cordis.europa.eu/project/id/101101974`.

[6] Daniel Muradas Odriozola, Sylvie Marquier, Joseph Morlier, and Christian Gogu. Control surface sizing and design through integrated mdo approach: Enhancing load alleviation while preserving handling qualities. *International Forum on Aeroelasticity and Structural dynamics IFASD*, 2024.

[7] Martin R. Waszak and David K. Schmidt. Flight dynamics of aeroelastic vehicles. *AIAA*, 1988. doi: 10.2514/3.45623.

[8] D McLean and RA Prasad. A structure load alleviation control system for a large aircraft. *Transactions of the Institute of Measurement and Control*, 2(1):25–37, 1980.

[9] Jia Xu and Ilan Kroo. Aircraft design with maneuver and gust load alleviation. In *29th AIAA Applied Aerodynamics Conference*, page 3180, 2011. doi: 10.2514/6.2011-3180.

[10] Flávio J Silvestre, Antônio B Guimarães Neto, Rafael Mendes Bertolin, Roberto Gil Annes da Silva, and Pedro Paglione. Aircraft control based on flexible aircraft dynamics. *Journal of Aircraft*, 54(1):262–271, 2017. doi: 10.2514/1.C033834.

[11] Nicolas Fezans, Hans-Dieter Joos, and Christoph Deiler. Gust load alleviation for a long-range aircraft with and without anticipation. *CEAS Aeronautical Journal*, 10:1033–1057, 2019. doi: 10.1007/s13272-019-00362-9.

[12] Christian Wallace and Nicolas Fezans. Lidar-based gust load alleviation-increasing the load reduction potential through a two-degree-of-freedom controller architecture. In *20th International Forum on Aeroelasticity and Structural Dynamics (IFASD 2024)(SCOPUS)*, 2024.

[13] Hugo Fournier, Paolo Massioni, Minh Tu Pham, Laurent Bako, Robin Vernay, and Michele Colombo. Robust gust load alleviation of flexible aircraft equipped with lidar. *Journal of Guidance, Control, and Dynamics*, 45(1):58–72, 2022. doi: 10.2514/1.G006084.

[14] Matthias Wuestenhagen. Gust load alleviation control of aircraft with varying mass distribution. In *AIAA SCITECH 2023 Forum*, page 0371, 2023. doi: 10.2514/6.2023-0371.

[15] Sunpeth Cumnuantip, Matthias Schulze, and Wolf R Krüger. Assessment of the aeroelastic stability of high aspect ratio wing aircraft during the preliminary design. In *International Forum on Aeroelasticity and Structural Dynamics, IFASD 2024*, 2024.

[16] Hannes Wilke, Géfferson C Silva, and Flávio J Silvestre. Aileron-flap-integrated roll control law by optimized control allocation for flexible transport aircraft. In *ICAS 2024*, 2024.

[17] J. Ensor A. Pomfret and T. Clarke. Eigenstructure assignment for semi-proper systems: Pseudo-state feedback. *IFAC Proceedings Volumes, 38(1), 338-341*, 2005. doi: 10.3182/20050703-6-CZ-1902.00627.

[18] John Wiley & Sons, editor. *Aircraft Control and Simulation: Dynamics, Controls Design, and Autonomous Systems*. John Wiley & Sons, 2015. ISBN: 9781118870983.

[19] J. M. Feldwisch and M. Bauer. UltraFLoads: A simulation suite and framework for high-fidelity flight loads, 2023. `https://elib.dlr.de/194250/`.

[20] A. A. G. Quesada, P. J. Gonzalez, G. C. Barbosa, G. Stavorinus, and F. J. Silvestre. Influence of nonlinear aerodynamic effects on high aspect ratio aircraft model. *International Forum on Aeroelasticity and Structural dynamics (IFASD)*, 2024. Last review on 05.02.2025.

[21] Flávio J Silvestre and Robert Luckner. Experimental validation of a flight simulation model for slightly flexible aircraft. *AIAA Journal*, 53(12):3620–3636, 2015. doi: 10.2514/1.J054023.

[22] Flávio J. Silvestre and Pedro Paglione. Dynamics and control of a flexible aircraft. *AIAA*, 2008. doi: 10.2514/6.2008-6876.

[23] Flávio Jose Silvestre. *Methodology for Modelling the Dynamics of Flexible, High-Aspect -Ratio Aircraft in the Time Domain for Aeroservoelastic Investigations*. Mensch und Buch Verlag, 2012. ISBN: 978-3-86387-316-5.

[24] L Dehmlow, PJ González, G Stavorinus, AA García Quesada, and FJ Silvestre. *Aircraft with Folding Wingtips Dynamics Model Based on Lagranges Method*. Deutsche Gesellschaft für Luft-und Raumfahrt-Lilienthal-Oberth eV, 2025.

[25] B. G. d. O. Silva and W. Mönnich. System identification of flexible aircraft in time domain. *AIAA p. 4412*, 2012. doi: 10.2514/6.2012-4412.

[26] Zeinab Eltaher. *Modelling and Implementation of a Real-Time Flexible Aircraft Simulation Environment with Animation of Flight Path, Attitude and Airframe Deformation*. Master thesis, Technical University Berlin, Berlin, 2024. `https://zenodo.org/records/15012245`.

[27] Gefferson C Silva, Bernd Boche, Hannes Wilke, and Flávio J Silvestre. On the preparation of a flexible real-time aircraft model for a flight simulator. *International forum on aeroelasticity and structural dynamics*, 2024.

[28] MSC Software Corporation. *MSC Nastran: Quick Reference Guide*. MSC Software Corporation, 2021. Version 2021.1.

[29] Willi Mickein, Ralf Alberto Senger Franco, Alvaro Antonio Garcia Quesada, Pedro Jose González, Flávio Jose Silvestre, Kilian Streitenberger, and Wolf-Reiner Krüger. Numerical validation of a high-aspect ratio wing flexible aircraft model. Technical report, Technische Universität Berlin, 2025.

[30] EASA, editor. *CS25 European Union Aviation Safety Agency: Certification Specifications 25 – Large Aeroplanes*. EASA, 2023.

[31] USAF, editor. *United States Department of Defense: Detail Specification: Flight Control Systems-Design. (MIL-DTL-9490E)*. USAF, 2008.

[32] USAF, editor. *United States Department of Defense: Flying Qualities of Piloted Aircraft. (MIL-STD-1797)*. USAF, 1995.

[33] H. Wilke. TN-FMRA 2024-001.v1 Auslegung des Bahnreglers für das Referenzflugzeug im Forschungsprojekt WISDOM. Technical report, Technische Universität Berlin, Issue 1, 19.06.2024.

[34] B. Boche H. Wilke, G. Silva and F. J. Silvestre. Allgemeine Bahnreglung Zwischenergebnisse Januar 2024. Technical report, Technische Universität Berlin, Issue 1, 30.01.2024.

[35] F. Stalla, T. Kier, and A. Eberle. UP Wing, D2.3.1-5 Basic Control Law for Load Control. Technical report, Airbus/DLR, 2023. Issue 1, 28.03.2023.

[36] Pedro J González, Flávio J Silvestre, Mateus de Freitas Virgilio Pereira, Zi Yang Pang, and Carlos ES Cesnik. Loop-separation control for very flexible aircraft. *AIAA Journal*, 58(9):3819–3834, 2020. doi: 10.2514/1.J058692.

[37] USAF, editor. *Background Information and User Guide for MIL-F-8785C, Military Specification Flying Qualities of Piloted Airplanes*. Air Force Wright Aeronautical Laboratories, 1982.

[38] Rafael M Bertolin, Antonio B Guimaraes Neto, Guilherme C Barbosa, Juliano A Paulino, and Flávio J Silvestre. Design of stability augmentation systems for flexible aircraft using projective control. *Journal of Guidance, Control, and Dynamics*, 44(12):2244–2262, 2021. doi: 10.2514/1.G005783.

[39] Vega Handojo. *Contribution to load alleviation in aircraft pre-design and its influence on structural mass and fatigue*. PhD thesis, Technische Universität Berlin, 2021. `https://elib.dlr.de/139558/`.

[40] U. Scholz, U. Thiessen, and B. Stefes. UP Wing, D1.1.1-5 Wing movables architecture baseline configuration DLR-F25. Technical report, Airbus, Issue 1, 13.02.2023.

[41] Kilian M Streitenberger and Johan M Feldwisch. CFD-based aeroelastic maneuver and gust loads analysis for a high aspect ratio wing configuration. In *AIAA SCITECH 2025 Forum*, page 1663, 2025. doi: 10.2514/6.2025-1663.

[42] R.J. Guyan. Reduction of stiffness and mass matrices. *AIAA Journal, Vol.3, No.2*, 1964. doi: 10.2514/3.2874.

[43] Pedro Gonzalez, Gerrit Stavorinus, Flávio J Silvestre, Arne Voß, Yasser M Meddaikar, and Wolf Krueger. TU-flex: A very-flexible flying demonstrator with a generic transport aircraft configuration. In *AIAA Scitech 2023 Forum*, page 1312, 2023. doi: 10.2514/6.2023-1312.

[44] M. Drela and H. Youngren. Athena vortex lattice, 2017. Last review on 05.02.2022. `https://web.mit.edu/drela/Public/web/avl/`.